Fatigue crack growth characterization of composite-to-steel bonded interface using ENF and 4ENF tests

Feng, Weikang; Arouche, Marcio Moreira; Pavlovic, Marko

DOI
10.1016/j.compstruct.2024.117963

Publication date
2024

Document Version
Final published version

Published in
Composite Structures

Citation (APA)
Feng, W., Arouche, M. M., & Pavlovic, M. (2024). Fatigue crack growth characterization of composite-to-steel bonded interface using ENF and 4ENF tests. *Composite Structures*, *334*, Article 117963. https://doi.org/10.1016/j.compstruct.2024.117963

Composite Structures 334 (2024) 117963

Contents lists available at ScienceDirect

Composite Structures

journal homepage: www.elsevier.com/locate/compstruct

Fatigue crack growth characterization of composite-to-steel bonded interface using ENF and 4ENF tests

Weikang Feng, Marcio Moreira Arouche, Marko Pavlovic *

Faculty of Civil Engineering and Geoscience, Delft University of Technology, 2600AA Delft, the Netherlands

ARTICLE INFO

Keywords:
Fatigue debonding
ENF test
DIC
VCCT
Paris curves

ABSTRACT

In this paper, mode II fatigue crack growth properties of the composite-to-steel interface are characterised through different test configurations, namely ENF and 4ENF tests. Different loading types including force control and displacement control methods are compared. An innovative shear strain based method is proposed for monitoring the mode II crack growth at the bi-material interface through Digital Image Correlation (DIC). A 3D finite element model with Virtual Crack Closure Technique (VCCT) is built and used for obtaining the strain energy release rate (SERR) to investigate the effect of geometrical nonlinearity, friction at the interface and steel yielding, as well as to verify the mode mixity. The results show that the standard 3-point bending ENF specimen can be unstable under force control and sweeps narrow SERR range by a single test under displacement control. The 4-point bending 4ENF test shows stable crack propagation and clear SERR developing trend. More pronounced geometrical nonlinearity and friction effect exist for 4ENF test which can be considered when interpreting the Paris curves by a nonlinear finite element model.

1. Introduction

Composite materials have been increasingly used in demanding engineering applications due to their light weight, flexibility, high fatigue and corrosion resistance. One of the most promising usage of composites in structures is the composites-to-metal hybrid structure. It has been widely used in traditionally metal-based industries such as aerospace industry [1], automotive industry [2] and now is increasingly used in construction industry [3] for strengthening existed structures [4,5] and connecting elements in new structures. The integrity of the hybrid structures heavily depends on the performance of composite-to-metal connections. Among different joining techniques, bonded joint is preferred for the connections as it provides enhanced stress transfer mechanisms and design flexibility [6]. However, the connections are prone to fail under certain circumstances. For instance, the wrapped composite joints investigated by the authors [7–9], where steel hollow sections are connected by composite wrap, were found to experience debonding failure at the composite-to-steel interface under fatigue loading. It is crucial to characterise the crack growth behaviour at the interface for predicting fatigue behaviour at the joint level. Fracture mechanics method has been developed to evaluate the performance and assist design of bonded joints such as in Ref. [4,5,10]. Typical failure modes of the bonded joints include mode I (resulting from peel stress), mode II (resulting from in-plane shear stress) and mixed mode debonding [11]. While mode I fracture and fatigue crack growth behaviour has been widely investigated [12–16], the mode II behaviour requires further studies.

Different test configurations have been developed for evaluating mode II fracture behaviour within composite layers or bonded interfaces [6,17]. The most commonly used configuration is the end-notched flexure (ENF) test [15], which has been standardized for determination of interlaminar fracture toughness of unidirectional FRP matrix composites [19]. However, the ENF specimen is prone to unstable crack propagation if designed inappropriately and the transverse shear effect at the crack region may deviate the obtained mode II fracture toughness from the true value [18,20]. Recently, another configuration, namely the 4-point bending end-notched flexure (4ENF) test, have been developed [21,22]. This allows constant bending moment between its two loading points and leads to stable crack propagation such that the whole fracture resistance curve (R-curve) can be obtained. Despite the stable characteristic of 4ENF tests, it is reported that the obtained fracture toughness can be 20–40 % higher than that obtained by ENF tests [22].

Schuecker et al. [23] evaluated the mode II delamination toughness from ENF and 4ENF tests numerically. It was found out that the friction

* Corresponding author.
E-mail address: M.Pavlovic@tudelft.nl (M. Pavlovic).

https://doi.org/10.1016/j.compstruct.2024.117963
Received 27 July 2023; Received in revised form 2 January 2024; Accepted 6 February 2024
Available online 7 February 2024

effect is larger in the 4ENF than ENF testing configuration. For 4ENF tests, the friction effect is more pronounced with increasing inner span length, but not large enough to explain the difference between the fracture toughness obtained from ENF and 4ENF tests. The difference results mainly from errors when determining crack length and specimen compliance during a 4ENF test [24]. Davidson et al. [25,26] investigated the effects of friction and geometry on the perceived toughness from ENF and 4ENF tests by linear and nonlinear finite element (FE) modelling. Results showed that the effect of geometrical nonlinearity is more pronounced in 4ENF than in ENF tests. The fracture toughness obtained from 4ENF test model with a friction coefficient $\mu = 0.5$ can be 12–15 % lower than the results of a frictionless model ($\mu = 0$), while for ENF specimens the difference between these two models is less than 7 %.

Recently, the usage of ENF and 4ENF configuration has been extended for the fracture characterization of bi-material bonded joints. In bi-material interfaces, one critical issue is to achieve pure mode II fracture at the crack tip or to partition the mode I and mode II components if mode mixity exists [6]. Dadej et al. [27] compared the rigid interface model [28] and the elastic interface model [29] in terms of interpreting critical SERR of asymmetric ENF tests on glass-fiber metal laminates. Jiang et al. [30] employed the 4ENF test to evaluate the mode II fracture behaviour for adhesively bonded composite-steel joints. Specimens were designed to have the same bending stiffness for the upper and lower adherends to achieve pure mode II behaviour. The SERR values are calculated based on the extended global method (EGM) [31] and the results were found to be comparable with that obtained by the virtual crack closure technique (VCCT). Meanwhile, Ouyang et al. [32] proposed a bi-material ENF test configuration where the two arms have the same longitudinal strain distribution at the faying surfaces, instead of having the same bending stiffness, to remove the normal deformation components related to mode I fracture behaviour. It can be seen that no consensus has been made on this issue.

Although the mode II fracture behaviour has been extensively investigated under quasi-static loadings, there are limited research carried out to evaluate fatigue delamination or debonding resistance. Existing research mainly focus on the fatigue crack growth (FCG) within composite layers. Matsubara et al. [33] investigated the mode II FCG from delamination of glass fiber reinforced polymers (GFRPs) by ENF tests. The tests were conducted under decreasing-load and constant-load in UD (unidirectional tape) and C (UD plus satin-woven fabric) laminates. It is found that fiber bridging had little or no influence on mode II fatigue crack growth. Brunner et al. [34] performed the displacement control ENF test to build the fatigue delamination resistance curves for FRP-matrix laminates. The results showed that the fatigue crack growth resistance is independent of the loading frequency. In addition, it is crucial to prevent specimens from shifting during the test. Carreras et al. [35] pointed out that, due to the non-monotonic evolvement of the SERR, in constant displacement control ENF tests, the range of crack growth curve covered by a single test is narrow, thus requiring a batch of several specimens to be tested under different severity (G_{II}/G_{IIcrit}) conditions in order to fully characterize the crack growth. They proposed a variable displacement test procedure with constant negative SERR gradient throughout crack propagation, through which the range of severities covered by a single test can be increased to the desired range of 0.1–0.45. Shindo et al. [36] conducted fatigue 4ENF tests for woven GFRP under displacement control. The maximum displacement was chosen to be 80 % of the static critical displacement. The VCCT was used to calculate the SERR around the crack tip with and without friction coefficient considered.

Limited work has been performed to characterise the mode II fatigue behaviour at bi-material bonded interfaces. Bieniaś et al. [37] characterised the FCG of CFRP and GFRP fiber metal laminates in mode II by force control ENF tests. Tests were conducted at different load levels and the similitude of the maximum SERR is utilised. Adamos et al. [38] successfully characterized the mode II fatigue behaviour of Titanium/CFRP adhesive joints based on displacement controlled ENF tests. They found out that a proper full cubic polynomial for the compliance calibration can avoid reducing the inspected SERR range. The results also showed that the FCG is insensitive to the employed similitude parameter and residual thermal stress effect. Overall, the existing research related to the mode II behaviour mainly focused on fracture and fatigue crack growth within composite layers. Research carried out to characterize fracture and fatigue crack growth at the bi-material interface is mainly limited to fiber-metal laminates. There is still no research for characterising fatigue crack growth at composite-to-steel interfaces. Furthermore, there is no systematic comparison among different testing geometries and loading protocols.

This work aims at characterising the mode II fatigue crack growth behaviour at the composite-to-steel interface considering different test configurations. The ENF and 4ENF testing methods are evaluated under force control and displacement control. A crack length monitoring method based on digital image correlation (DIC) is proposed. The SERR is determined analytically by the EGM, and numerically by the VCCT. Finally, the advantages and limitations of the testing configuration, including the effect of friction, are investigated using Paris curves.

2. Experimental set-up

2.1. Specimens

The ENF and 4ENF specimens are designed with the same geometry. Nominal dimensions of the specimens, including the width (B), half-span (L), load-to-support point distance (L_a), upper and lower arm thicknesses (h_1 and h_2) and the pre-crack length (a_0), are shown in Fig. 1 and Table 1. A total of 12 specimens were tested, with 3 identical specimens for 4 test configurations. For the bi-material specimen, the thicknesses of steel and composite arms are designed to meet the decoupling condition described in **Eq.** (1), such that pure fracture modes can be obtained according to Ref. [6,32].

$$E_1 h_1^2 = E_2 h_2^2 \tag{1}$$

where E_1 and E_2 are the elastic modulus in the longitudinal direction for the upper and lower arms, respectively. The specimens are positioned with the steel arm on the top to maintain compressive stresses in the composite materials next to the interface under bending moments at the crack tip. The compressive stresses can provide confinement of the composite material thus prevent the crack to migrate into the composite layers[39,40].

Mild steel S355 is employed for the steel plate. The steel surface is grit blasted (with $S_q = 20.52$ μm [7]) and chemically degreased to ensure good bonding quality. A non-adhesive insert of 32 μm thickness is inserted at one end of the specimens to induce a pre-crack between steel and composite arms. The composite laminate is manufactured by hand lay-up of the glass fiber plies on the steel treated surface. As the composite laminate is directly applied on the steel plate, no separate adhesive layer was present at the interface. The composite ply is formed by woven interleaved with chopped strand mat (CSM) and a vinyl ester matrix system with fibre volume fraction of approximately 30 %. The lamination process occurs at controlled factory condition of 17 ± 1 °C and 50 ± 5 %RH. Specimens are cut from the plate (500 × 400 mm) using water jet with the designed width and then post-cured at 120 °C for 15 h. After that the white paint followed by a black speckle pattern is applied on one side of the specimens to facilitate crack monitoring by digital image correlation (DIC). The speckle size is kept between 0.2 and 0.3 mm corresponding to 3-by-3 and 7-by-7 pixels to achieve a good quality as investigated in Ref. [41], where the specimen scale is similar to that in the present study. The material properties of composite laminate are obtained by standard tensile/compressive/in-plane shear coupon tests according to ISO 527–1 [42], ISO 14126 [43] and ISO 14129 [44] respectively and are summarised in Table 2. More details related to the material test can be found in Ref. [45].

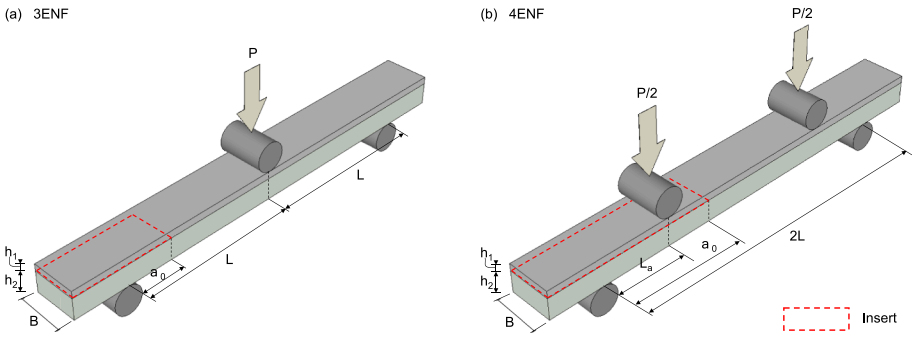

Fig. 1. Schematic of ENF and 4ENF tests.

Table 1
Test specimens.

Specimen type	Loading type	Loading Frequency (Hz)	Specimens	Dimensions (mm)					
				h_1	h_2	B	L	L_a	a_0
ENF	Force control	4	ENF-F-1/2/3	3	12	25	137	–	67
	Displacement control		ENF-D-1/2/3						
4ENF	Force control		4ENF-F-1/2/3	3	12	25	137	52	67
	Displacement control		4ENF-D-1/2/3						

Table 2
Material properties of the composite laminate.

Mechanical property	Average value and (CoV [%])
Longitudinal and transverse compressive strength – $f_{x,c} = f_{y,c}$	200 MPa (3.79)
Longitudinal and transverse compressive modulus – $E_{x,c} = E_{y,c}$	12077 MPa (4.50)
Longitudinal and transverse tensile strength – $f_{x,t} = f_{y,t}$	216.2 MPa (5.78)
Longitudinal and transverse tensile modulus – $E_{x,t} = E_{y,t}$	11798 MPa (6.37)
In-plane shear strength – τ_{xy}	72.19 MPa (2.59)
In-plane shear modulus – G_{xy}	3120 MPa (6.81)

2.2. Test set-up, instrumentation and loading protocol

The tests are conducted in a universal testing machine coupled with a 15 kN load cell. The test set-up is shown in Fig. 2. In the ENF tests, specimens are loaded by a single load in the section of half-span, while in the 4ENF tests two symmetric load points are distributed by a loading beam connected to the actuator by a pin such that the two loading points can contact the top surface of the specimen perfectly during the tests. A digital camera with 51 MPx is positioned perpendicular to the specimen, serving as the 2D DIC system for monitoring crack propagation during the tests. During the tests, the camera is controlled by the testing machine. The cyclic loading is stopped every 500 cycles, or 1 % stiffness degradation, then photos are taken at the minimum and maximum forces (or displacements), respectively.

The fracture behaviour was previously characterised from static 4ENF specimens manufactured by the same materials [46]. The SERR obtained at crack initiation, $G_{II,ini}$, is equal to 1.12 N/mm, and the load is 3.37 kN. No static ENF tests were conducted due to its inherent instability. The critical load is back calculated based on the extended global method (EGM, see section 3.1) as to be 2.61kN, roughly assuming that the initial SERR values obtained by ENF and 4ENF tests are the same. Both displacement and force control configurations are used for the tests to compare the two different loading types. The load ratio, or the displacement ratio, is kept as 0.1 with the loading frequency being 4 Hz for all tests. For both force control and displacement controlled ENF tests, the tests are started with the SERR level of 16 to 25 % of $G_{II,ini}$. The maximum force / displacement is back calculated accordingly. This value exceeds the threshold value sufficiently to induce substantial crack growth, and it is low enough to allow for the widest possible SERR since it will increase during the tests. For displacement controlled 4ENF tests,

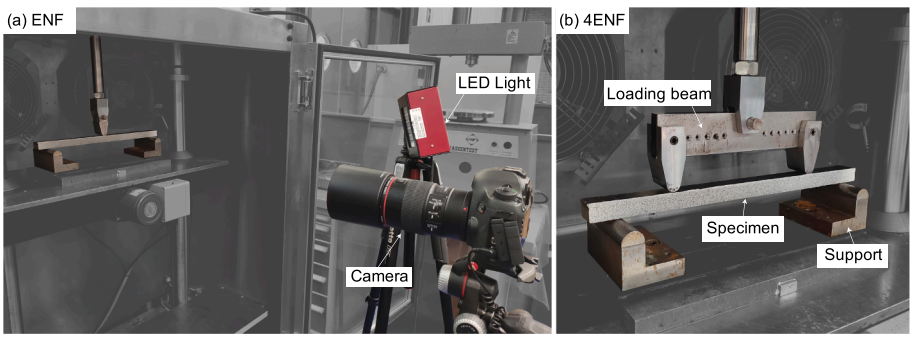

Fig. 2. Test set-up (a) ENF test; (b) 4ENF test.

a relatively high starting level of 49 to 64 % of the $G_{II,ini}$ is chosen to ensure significant crack growth (since the load decreases as the crack propagates) and low enough to avoid too rapid crack growth (e.g. 0.1 mm/cycle) for the convenience of crack monitoring. The same principle is applied for starting the force controlled 4ENF tests. Since the SERR level of 4ENF test is only determined by the applied force (according to Eq. (7) in section 3.1), a constant applied force will lead to a constant SERR level, corresponding to one point in the Paris curves. Therefore, the force is reduced manually by 5 % steps after every 5000 to 10,000 cycles during the test in order to construct the Paris curve with multiple points.

2.3. Crack length measurements

A widely used method for monitoring crack length, a, of an ENF specimen is the compliance calibration method (CCM) [36], where the crack length is estimated by an experimentally measured or theoretically calculated compliance. The CCM is popular in mode II fracture tests for not requiring optical measurements. However, compliance-based methods require that all the materials remain in linear elastic behaviour such that the compliance increases solely from the crack growth. Therefore, it is not applicable in the presence of material nonlinearity, e.g. steel yielding in the steel-to-composite bonded joint. The DIC technique has been widely used nowadays for monitoring cracking behaviour of concrete and composite materials due to its advantages of non-contact, full-field and real-time measurements. Monitoring the crack growth indirectly by analysing strains or displacements on the surface of the specimen, the DIC-based method is independent of material nonlinearity and can avoid tracking the crack tip visually. Now that the method has been applied for monitoring mode I fatigue crack growth in DCB specimens [47], it also has the potential to be applied in mode II fatigue crack growth in ENF specimens.

During the DIC analysis, the side of the specimen between the two supports (with the size of 15 × 274 mm) is selected and processed in the GOM ARAMIS software, where a subset size of 9 pixels in combination of step size of 5 pixels are chosen to meet the accuracy requirements according to Ref. [41]. The shear strain distributions are extracted from a surface curve defined on top of the interface in DIC, as shown in Fig. 3 (a), at the maximum load of each recorded cycle. Where there is a perfect bond between steel and composites, the shear strains at the interface remain nearly zero as shown in Fig. 3 (b). On the contrary, the shear strains increase due to relative movement between steel and composites once the interface debonds. The crack tip can be located by comparing the shear strains along the interface with a certain threshold, above which the interface is considered to be debonded. As the shear strain at the crack tip is influenced by the local bending moments at the crack tip in the arms of the notched flexure specimen imposed by the external loading, a calibration test is done firstly to find the relationship between the shear strain threshold level and total bending moment, M (as indicated in Fig. 3) at the crack tip. The assumption is that the local bending moment in the steel and composite arms of the notched flexure specimen, namely M_1 and M_2, are correlated to the total bending moment at the crack tip $M = M_1 + M_2$. During the calibration test, ENF and 4ENF specimens are loaded at levels below the critical force. The shear strains at the crack tip, namely the thresholds, under different bending moment levels are extracted as shown in Fig. 3 (b). A linear relationship between the threshold and moment at the crack tip is obtained, as shown in Fig. 3 (c). This fitted formula is then applied to the crack length measurements.

The procedure for crack length determination analysis is illustrated as a flowchart in Fig. 4. The shear strains along the interface are extracted at different cycles for each specimen, which serve as input for a script. Within each loop (corresponding to each recorded cycle), the crack length is determined by comparing the extracted strains along the interface with the strain threshold. As the crack grows, bending moment at the crack tip, thus the strain threshold, will change under both ENF and 4ENF test configurations. For ENF tests, the moment at the crack tip is determined by the force and the crack length. The threshold needs to be updated based on the force as well as the crack length obtained from the previous recorded cycle. For 4ENF tests, the moment at the crack tip is independent of the crack length, and the threshold is updated solely according to the force at that cycle. The procedure is looped until the last recorded cycle during the test. Two examples of threshold variation, for force controlled ENF and displacement controlled 4ENF specimens, are shown besides the flowchart in Fig. 4. The monitored crack growth results will be further discussed in section 4.2.

To benchmark the shear strain method, an alternative approach that relies on the relative displacement between two points on either side of the interface is utilized, which has been widely adopted and validated in the literature [31,48]. As shown in Fig. 5 (a), pairs of virtual points are marked on the upper and lower arms at sections of 2 mm intervals along the interface. The relative displacements between these two points are plotted against photo numbers in Fig. 5 (b). When the relative movement exhibits a drastic increase, it is considered that the crack reaches

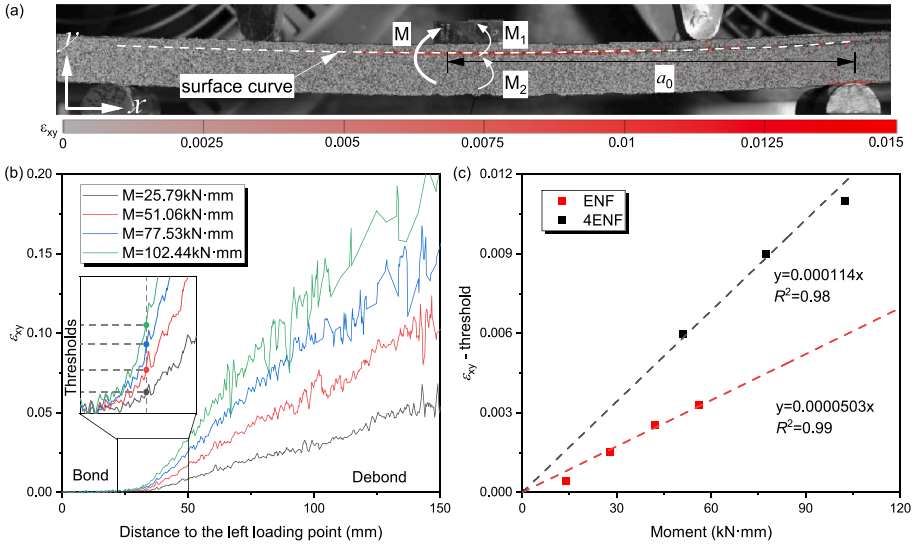

Fig. 3. Shear strain threshold for determining crack length (a) contour plot of shear strain from DIC; (b) shear strain distribution along the interface at different moment levels; (c) relationship between shear strain threshold and moment.

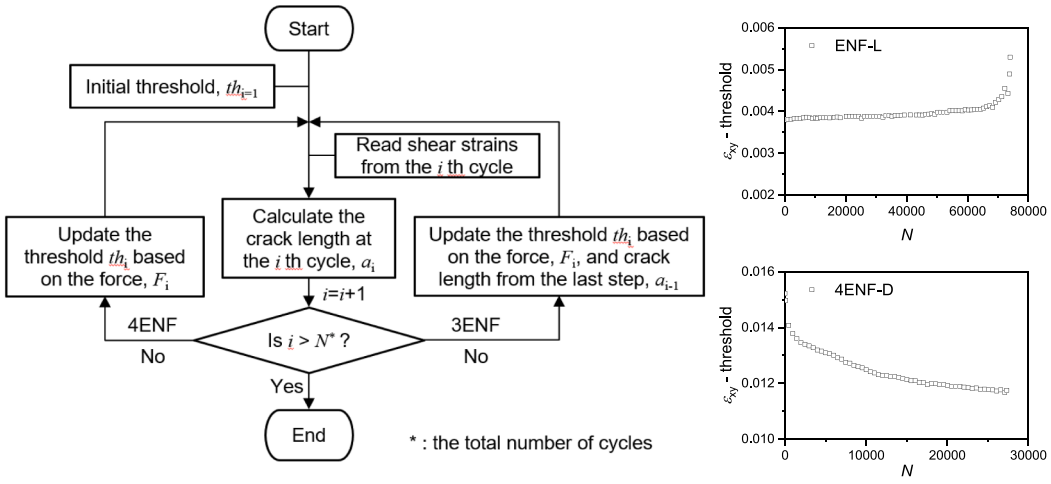

Fig. 4. Flowchart for script in MATLAB and examples of threshold variation.

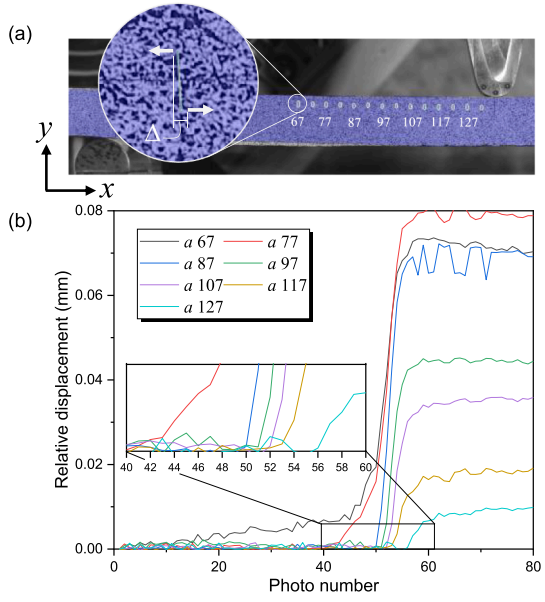

Fig. 5. Displacement measurements for determining crack length.

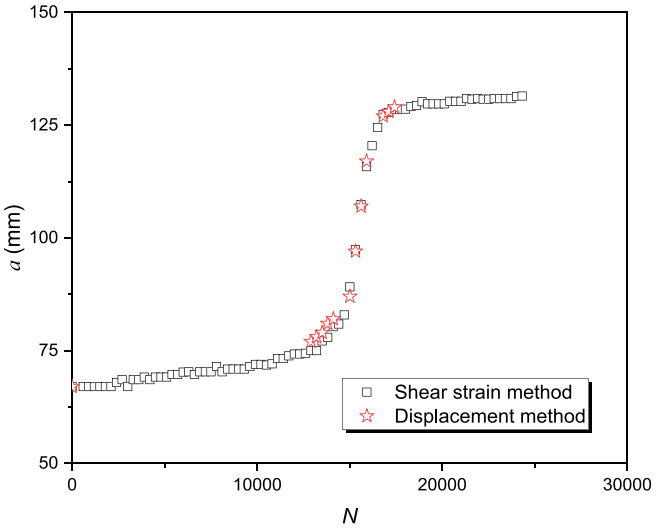

Fig. 6. Comparison between shear strain and displacement methods.

the section of these points. For instance, the crack reaches 87 mm at the photo number of 50, corresponding to 15,011 cycles.

Crack lengths obtained by the shear strain method and the relative displacement method in a ENF test are compared in Fig. 6. The two results exhibit a high degree of overlap, providing validation of the strain method for crack length monitoring. However, the displacement method is not able to monitor the crack growth for a short crack length. This can be seen in Fig. 5 at the sections of 67 and 77 mm. Furthermore, the shear strain method can track the strain field along the entire interface while the displacement method can only track the relative displacements at a limited number of specific locations. The following analysis will adopt the shear strain method.

3. Fracture data analysis

3.1. Extended global method

The crack driving force, namely the strain energy release rate (SERR), can be obtained by different methods. Williams [49] proposed the global method for calculating the energy release rate from the local values of bending moments and loads in a cracked laminate. Moslem, et al. [31] extended this method in order to consider the situation of asymmetric crack which lies between two different orthotropic layers. According to the extended global method (EGM), the mode II SERR can be calculated as follows:

$$G_{II} = \frac{M_{II}^2}{2BE_1 I_1}[1 + \psi - \xi(1+\psi)^2] \tag{2}$$

$$M_{II} = \frac{M_1 + M_2}{1 + \psi} \tag{3}$$

where M_{II} is the bending moment corresponding to mode II, M_1 and M_2 are the bending moments acting on the upper and lower arms at the crack tip as illustrated in Fig. 3 (a), ψ and ε are the bending stiffness ratios of arms for the specimens, which can be calculate by:

$$\psi = \frac{E_2 I_2}{E_1 I_1} \tag{4}$$

$$\xi = \frac{E_1 I_1}{(EI)_{eq}} \tag{5}$$

In **Eq.** (2), (3), (4) and (5), I_1 and I_2 are the moment of inertia of the upper arm and lower arm, respectively. $(EI)_{eq}$ is the equivalent bending stiffness of the specimen.

According to Fig. 1, the total bending moment at the crack tip for ENF test, namely $M_1 + M_2$, equals to $Pa/2$, while for 4ENF test, the total bending moment at the crack tip equals to $PL_a/2$. Substitution of these into **Eqs.** (2) and (3) leads to:

$$G_{II,ENF} = \frac{P^2a^2}{8BE_1I_1}\left(\frac{1}{1+\psi} - \xi\right) \tag{6}$$

$$G_{II,4ENF} = \frac{P^2L_a^2}{8BE_1I_1}\left(\frac{1}{1+\psi} - \xi\right) \tag{7}$$

3.2. Finite element method

Another commonly used method for obtaining SERR at the crack tip is using FE model by means of virtual crack closure technique (VCCT), which can also be used for obtaining the fracture mode ratio. This method assumes that the energy required to open a crack is the same as the energy required to close it [50]. Based on VCCT, a 3D finite element model is built in explicit solver of ABAQUS software [51] as shown in Fig. 7 (taking the 4ENF model as an example). The geometry and boundary conditions of the FE model follow the design of the ENF and 4ENF specimens, as shown in Fig. 1, while specimen dimensions are taken as the average measured values. Linear, hexahedron 8-noded solid elements with reduced integration (C3D8R) are used for both steel and composite parts. The mesh topology of the model is shown in Fig. 7.

Plasticity model in ABAQUS is used in the study to consider possible steel yielding, where elastic constants ($E = 210$ GPa, and $\upsilon = 0.3$) and nominal yield and ultimate stress (S355, $f_y = 355$ MPa, $f_u = 510$ MPa) in combination with isotropic hardening are defined. The composite laminate is modelled as one piece of solid part in this model. Stresses in the composite wrap in the cyclic load (fatigue) tests are much lower than the strength of the material shown in Table 2 according to the preliminary FE analysis. Therefore, the composite laminate is modelled with elastic material properties. Transversely anisotropic material properties are defined based on the tests results shown in Table 2 for the in-plane properties of the laminate: E_1, E_2, G_{12} and υ_{12}. In absence of test data, the out-of-plane elastic properties of the laminate, E_3, G_{13}, G_{23}, υ_{13}, υ_{23} are determined from the Classical Laminate Theory for an equivalent unidirectional material with the fibre volume fraction conforming of the tested laminate ($V_f = 30$ %).

A mesh sensitivity study is performed using a model with $a = 67$ mm. Different meshes with element length Δa of 0.5 mm, 1 mm, 1.5 mm and 2 mm and aspect ratio 1 are evaluated. The results of mode I/II/III SERR at the crack tip are extracted and normalized to 1 kN as shown in Fig. 8. It is shown in Fig. 8 (b) and (c) that mode II and III SERR converges for different mesh sizes. The mode I SERR is increasing as the mesh size decreases. This lack of convergence for mode I is assumed insignificant considering the negligible contribution from mode I fracture component. Taking the convergence of SERR values and computing efficiency into account, mesh size of 1 mm is chosen for the following analysis. The mode mixity at the crack tip will be further discussed in section 5.2.

4. Test results

4.1. Failure mode

Fig. 9 shows the side view of all the failed specimens. It can be seen that after experiencing cyclic loads, the steel plates exhibit different levels of plastic deformation. This is a typical difference between pure composite joints and hybrid composite-to-steel joints. In such case, the compliance calibration method (CCM) is not able to determine the crack length and calculate SERR. The first specimen of each series are opened for further observation on the failed interface. It can be seen from Fig. 10 that, due to absence of separate adhesive layer, all specimens showed the adhesive failure at the composite-to-steel interface. The final crack tip representing the maximum crack length during the fatigue tests monitored by DIC is indicated by the red dash line in the figure, the right side of which forms when the specimens are opened after tests.

4.2. Crack growth and SERR development

Based on the method introduced in section 2.3, representative crack growth curves for different test configurations are extracted and shown in Fig. 11. The corresponding mode II SERR values obtained from EGM is also shown in the same figure for comparison and interpretation of the results. It can be seen from Fig. 11 (a) that crack of the force controlled ENF specimens grows slightly during most part of the fatigue tests and increases suddenly. This is because that the SERR values remain relatively low in the beginning but increase quadratically as the crack length increases, as determined by **Eq.** (6). It should be noted that the crack has already reached the middle of the specimen underneath the loading pin, namely $a = 137$ mm, after the test. The unstable crack growth near the end makes it difficult to take pictures by the DIC system at high crack growth rates. In such circumstance, the crack length is only monitored until 94 mm. Moreover, one of the force controlled ENF specimens (ENF-F-3) failed abruptly before showing stable crack growth and, therefore, no optical image is recorded.

Fig. 11 (b) shows the crack growth and SERR development of displacement controlled ENF tests. It can be seen that, under such specimen geometry and test configuration, the crack development starts at a low rate and grows rapidly until it stabilizes near the loading pin ($a = 137$ mm). This particular trend comes from the combined increasing crack lengths and decreasing forces during the test and results in the increasing then decreasing SERR values, as indicated in the figure. The decreasing crack growth rate at later stages also comes from compressive stress in the through-thickness direction when the crack approaches the loading pin [35,37]. It is recommended that crack extension within 2 h (in this case $h_1 + h_2 = 15$ mm) from the load point should be

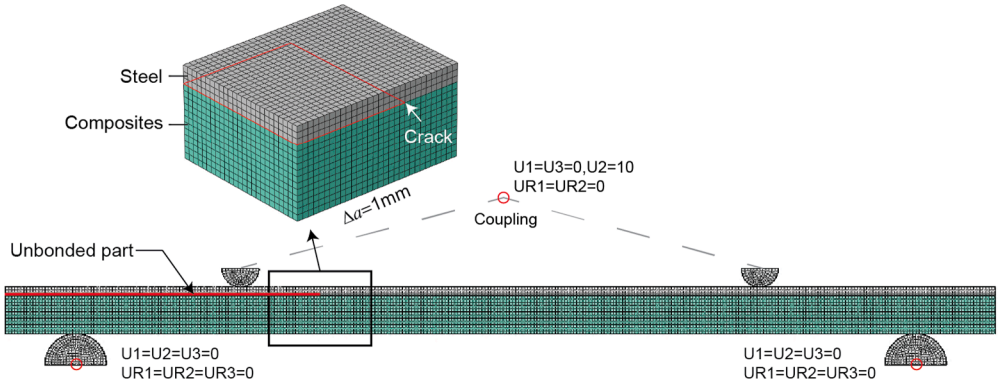

Fig. 7. Boundary conditions and mesh topology of the FE model – 4ENF model as an example.

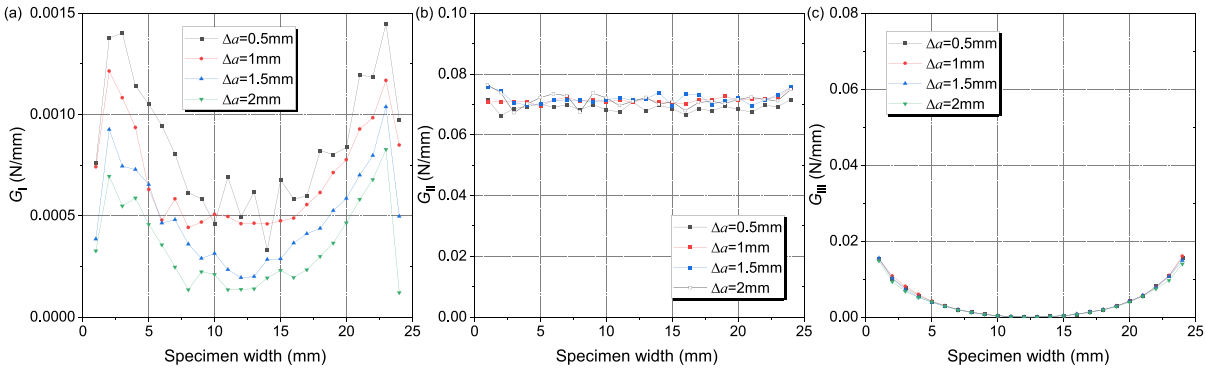

Fig. 8. Mesh size sensitivity study.

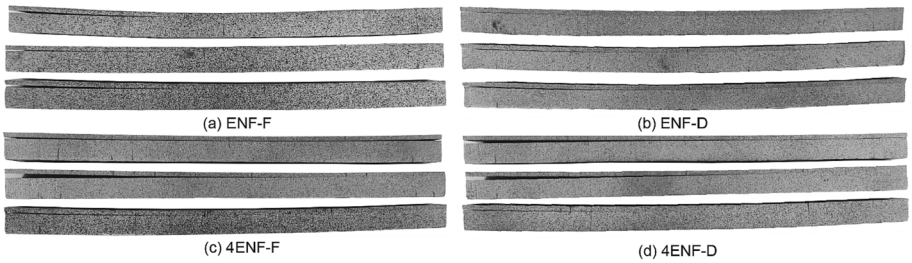

Fig. 9. Side view of failed specimens.

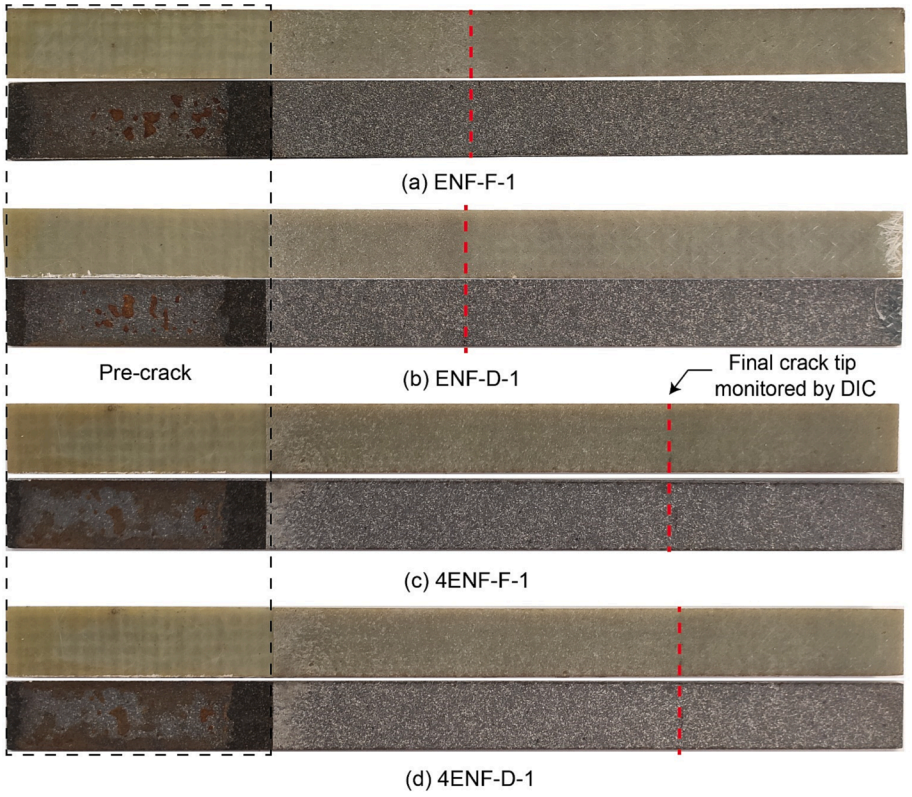

Fig. 10. Interface of failed specimens.

disregarded due to the influence of local compressive stresses [52]. In such case, the maximum valid crack length for ENF specimens is 122 mm. This non-monotonic behaviour of the SERR provides only small segments of the Paris curve by a single test [35]. Usually, a specific geometry or loading protocol needs to be designed, or different displacement levels be used to construct the entire Paris curve [35].

The SERR of 4ENF specimen is determined directly by the applied forces, as indicated by **Eq.** (7). Under force control, the SERR values exhibit stepwise decrease when the force is decreased manually in steps, as shown in Fig. 11 (c). The crack growth rate at each corresponding

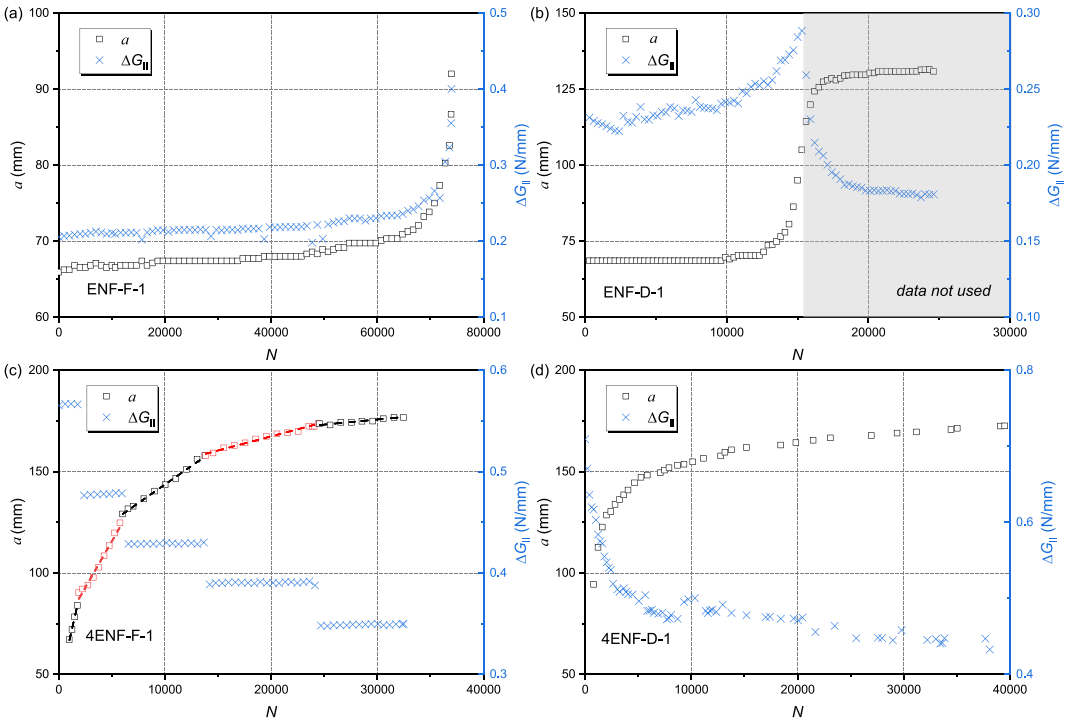

Fig. 11. Representative crack growth and SERR development curves from (a) force controlled ENF test; (b) displacement controlled ENF test; (c) force controlled 4ENF test; (d) displacement controlled 4ENF test.

force level is nearly constant and decreases accordingly. Under displacement control, the force level decreases gradually leading to gradual decrease of SERR, as shown in Fig. 11 (d). The crack growth rate also decreases and stabilizes at later stages. The 4ENF tests are stopped when the measured stiffness stabilized and no further crack extension is observed. Similar to the ENF tests, measured data from the region near the load points are disregarded, leading to the maximum valid crack length for 4ENF specimens as 207 mm. The maximum crack lengths within the valid range for all the specimens are summarised in Table 3. It can also be seen from Table 3 that the maximum SERR range covered by a single force controlled ENF test remains between 0.20 and 0.48 N/mm while the maximum range of SERR covered by a single displacement controlled ENF test stays around 0.25–0.33 N/mm. For the 4ENF test, the range can be as higher as 0.52–0.80 N/mm by force control and 0.35–0.76 N/mm by displacement control. The difference of SERR range among different test methods will be further discussed in the next sections.

4.3. Paris curves

The crack growth rate, da/dN, is calculated by the 7-point incremental polynomial method according to [53] for all the tests except for force-control 4ENF. The fitted crack length corresponding to the middle of the 7 points is used to calculate the SERR. For force controlled 4ENF test, linear fits on each crack growth segment is applied for calculating the constant crack growth rate, and the average SERR at each force level is used.

Based on the mode II SERR calculated by EGM and the crack propagation rates, the mode II fatigue debonding resistance curves, namely the Paris curves, are obtained from the 4 different test configurations, as shown in the log–log plot of Fig. 12. The test data points are fitted by a power law described in **Eq.** (8):

$$da/dN = C(\Delta G_{II})^m \tag{8}$$

where the similitude parameter ΔG_{II} is used. C and m values represent the intercept and slope of the curves respectively, and can be obtained by curve fitting using the least squares method. Arrows in the figure indicate the acquisition order of the data points during the tests. The fitted Paris curve parameters based on EGM, C and m, are summarised in Table 4. Except for the force controlled 4ENF specimens, where each individual specimen yields distinct results from one another, results of other types of specimens are fitted as a whole piece.

As shown in Fig. 12, the Paris curve of each type of specimens shows different scattering levels, which can also be reflected by the coefficient of determination, R^2, in Table 4. Displacement controlled 3ENF tests showed a relatively narrow range of SERR, which reflects on a relatively higher scatter, with $R^2 < 0.5$. The most consistent result applies to the force controlled 4ENF tests, with $R^2 > 0.91$, where only a small amount of data points are obtained from the average of several data points in each test of a certain force level. However, it should be noted that curve fitting was conducted for results from multiple specimens except for force controlled 4ENF test. The scatter comes from not only crack growth rate variations within one specimen but also varied properties of different specimens.

It can also be seen from Fig. 12 and Table 4 that each test configuration yields reproducible results. Comparing specimens from different test configurations, the fitted m values are in the same magnitude

Table 3
Summary of SERR range and crack length.

Specimen	F_{max} (kN)	$G_{II,min}$ (N/mm)	$G_{II,max}$ (N/mm)	a_{max} (mm)
ENF-F-1	1.13	0.22	0.39	91
ENF-F-2	1.13	0.2	0.48	105
ENF-F-3	–	–	–	–
ENF-D-1	1.17	0.25	0.32	119
ENF-D-2	1.14	0.25	0.33	121
ENF-D-3	1.13	0.23	0.28	119
4ENF-F-1	2.41	0.4	0.57	177
4ENF-F-2	2.88	0.58	0.82	203
4ENF-F-3	2.85	0.52	0.8	207
4ENF-D-1	2.61	0.43	0.71	173
4ENF-D-2	2.79	0.39	0.67	192
4ENF-D-3	2.6	0.35	0.76	183

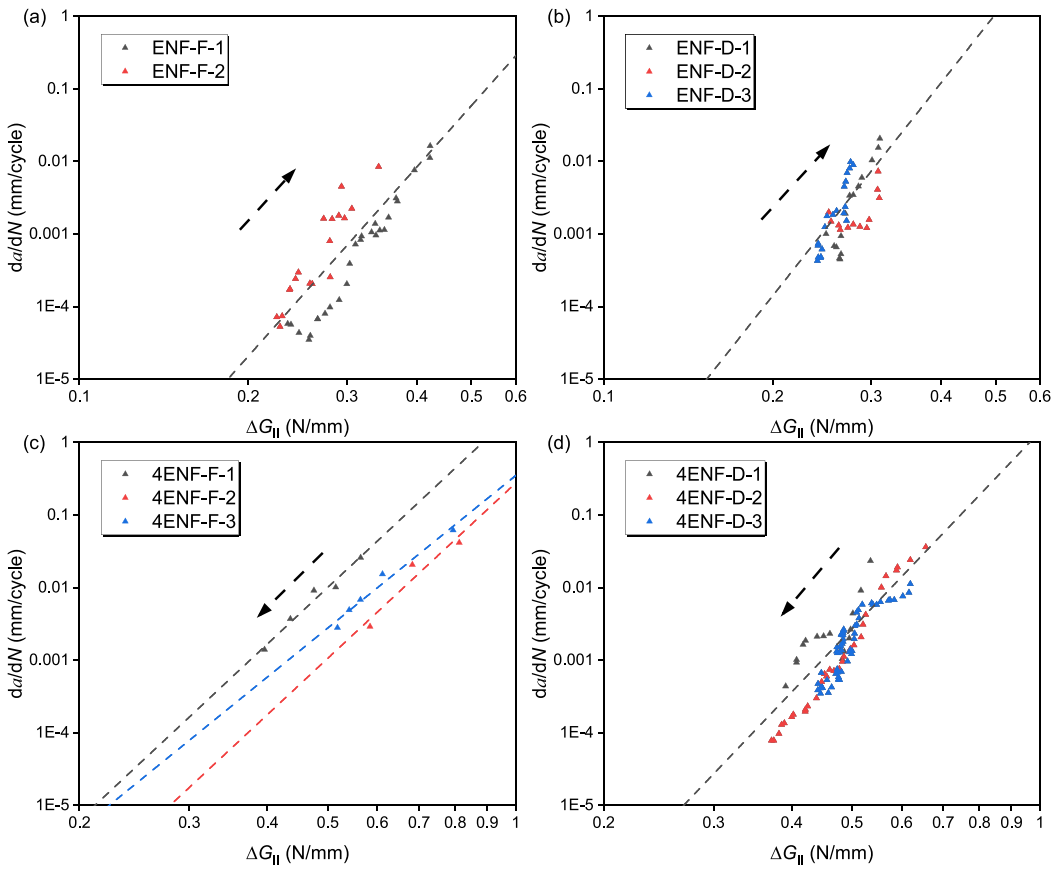

Fig. 12. Paris curves of (a) force control ENF tests, (b) displacement control ENF tests, (c) force control 4ENF tests, and (d) displacement control 4ENF tests.

Table 4
Summary of Paris curve parameters.

Specimen	EGM		FEA without friction		FEA with friction		R^2
	C	m	C	m	C	m	
ENF-F	23.96	8.68	36.48	8.80	44.27	8.80	0.81
ENF-D	939.00	9.77	23158.11	12.29	30338.01	12.29	0.44
4ENF-F-1	2.67	8.05	0.77	5.69	2.19	5.14	0.97
4ENF-F-2	0.28	8.02	0.32	6.63	1.55	6.18	0.91
4ENF-F-3	0.35	6.98	0.38	5.87	1.48	5.46	0.97
4ENF-D	1.41	9.02	1.57	7.61	14.92	8.49	0.85
ENF – all specimens	3.75	6.48	5.74	6.74	6.65	6.74	0.24
4ENF – all specimens	1.09	9.03	1.71	8.08	11.52	7.62	0.73

between 7 and 10. The fitted C values are in significant different magnitudes, with the maximum C value above 900 for ENF while the minimum value below 1 for 4ENF specimens. According to Eq. (8), C represents the crack growth rate at $\Delta G_{II} = 1$ N/mm. A higher C value reflects a lower fatigue resistance in the case of a constant m value. However, C values are sensitive to the slopes. A slight increase of m value may lead to a significant increase of C values, which is the case for ENF specimens. Results of all the specimens are plotted together in Fig. 13. Curve fits are applied for all the ENF specimens and 4ENF specimens, respectively. It can be seen that Paris curves of ENF specimens significantly shifted to the left compared with those of 4ENF specimens. This means that the fatigue resistance obtained by ENF is apparently lower than that obtained by 4ENF tests. Specifically, ΔG_{II} of ENF specimens can be up to 50 % lower than that of 4ENF specimens at the same crack propagation rate. The same trend is reported in literature [25,26,54], which stated that higher SERR values of 4ENF specimens resulted from the more pronounced geometrical nonlinearity and friction effects. A non-linear FE model is built in section 5.1 to explain this behaviour.

5. Discussion

5.1. Effects of friction and geometrical nonlinearity

The expectation is that the friction at the interface contributes to the load transferring mechanism and therefore reduced the SERR at the crack tip. In order to investigate the effect of friction at the interface, the friction coefficient between composite and steel fractured surfaces is measured. Samples are cut from the tested ENF and 4ENF specimens. The friction coefficient is measured by the tribometer (Rtec MFT-5000) in a parallel study using the same frequency as the fatigue tests, namely 4 Hz and found to be around 0.5 at the fractured interface between steel and composites.

The friction effects are taken into account in FE model. A penalty formulation with $\mu = 0.5$ is defined as the tangential contact behaviour in combination with VCCT between the steel and composite part in the FE model when friction effect is considered. Crack lengths of 67 (the initial crack length), 77, 87, 97, 107 mm are used for the ENF model and

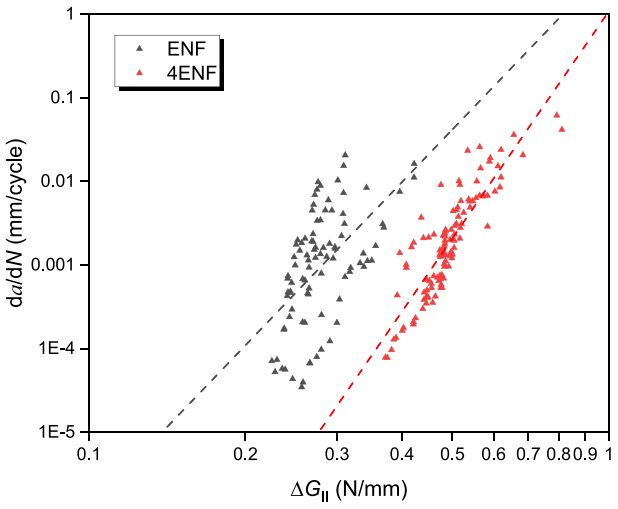

Fig. 13. Paris curves comparison between ENF and 4ENF tests.

G_{II} is extracted at load levels of 0.5, 0.7, 0.9, 1.1, 1.3 kN. For the 4ENF model, crack lengths of 67, 97, 127, 157, 187 mm are used and G_{II} is extracted at 1.5, 2, 2.5, 3, 3.5 kN. A nonlinear surface fit is applied to the results, thus establishing the relationship between SERR vs. force and crack length shown in Fig. 14. An equation with the same form as that of EGM (see **Eq.** (6)), namely $G_{II} = kP^2a^2$, is used to obtain the surface fit for the ENF model. In the 4ENF condition, literature states that G_{II} decreases as the crack increases due to possible geometrical non-linearity effect [25,26,54] which is not taken into account in the EGM. The influence of crack length is kept in the equation but with a linear relationship, namely $G = k_1P^2 + k_2a + k_3$, being accurate enough. The fitting parameters obtained from FE models without and with friction are summarised in Table 5**.** Substituting crack lengths and forces measured from experiments into the equations in Table 5, the G_{II} can be calculated by the FE models with or without the friction effect taken into account.

The Paris curves are reconstructed and compared with the EGM in Fig. 15. It can be seen from Fig. 15 (a) that the Paris curves obtained by EGM, FE model with and without friction overlap with each other for ENF specimens. This similarity can also be verified by the almost identical C and m parameters between these three methods in Table 4. This means that the geometrical nonlinearity and friction effect are not obvious for the ENF specimens. For the 4ENF specimens, however, Fig. 15 (b) shows that the Paris curve obtained by the FE model without friction already shifts to the left compared to that obtained by EGM. The same behaviour is also reported in literature [26] and is thought to be due to the more pronounced geometrical nonlinearity effect in the 4ENF configuration, i.e. the contact points (loading and support points) shift in such a manner as to reduce the bending moment in the arm while load is applied. This geometrical nonlinearity is not reproduced in a linear elastic model such as the EGM. When friction is considered, the SERR values becomes even significantly smaller, as also indicated by the increased C parameter (11.52) in Table 4. The more pronounced shift of curves observed in 4ENF indicates that the friction effect is more significant in 4ENF than in ENF [23,26]. This friction effect dissipates part of the energy during the fatigue cycles, thus reducing the SERR values at the crack tip.

A detailed analysis of the ENF and 4ENF test configurations is presented in Fig. 16. The contact pressure (CPRESS) along the cracked interface is extracted from ENF and 4ENF models at the same load level. It can be seen that a similar amount of contact pressure appears near the section of the left support point in both set ups. However, the 4ENF specimen shows a peak at the section of the left loading point. Although the ENF model displays a higher contact pressure near to the crack tip, the 4ENF model exhibits a larger amount of pressure between the cracked surfaces, causing lager friction forces than the ENF specimen due to the existence of a loading point at a cracked section. Therefore, more friction energy is dissipated in 4ENF than in ENF specimens during cyclic loadings.

Finally, Fig. 17 shows the Paris curves of ENF and 4ENF configurations considering the effects of friction and geometrical nonlinearity. It can be seen that these two data sets overlap well with each other. The average Paris curve parameters, shown in Table 4 ($C_{ENF} = 6.65$, $m_{ENF} = 6.74$ vs. $C_{4ENF} = 11.52$, $m_{4ENF} = 7.62$), are within the acceptable

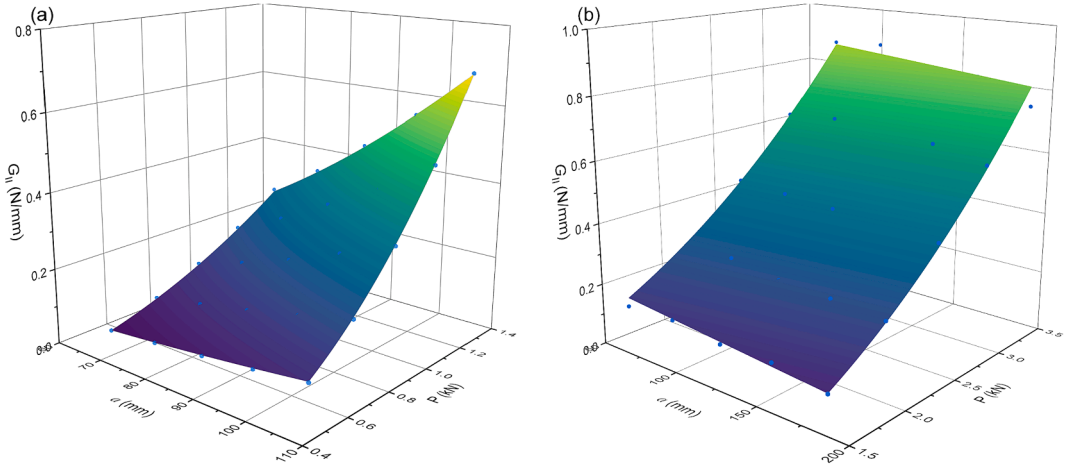

Fig. 14. SERR vs. force and crack length (a) ENF specimen; (b) 4ENF specimen with friction considered.

Table 5
Fitted results for SERR vs force and crack length.

Model	Equation	Coefficients		R^2	
		without friction	with friction	without friction	with friction
ENF	$G_{II} = kP^2a^2$	k = 3.68E-5	k = 3.54E-5	0.99	0.99
4ENF	$G_{II} = k_1P^2 + k_2a + k_3$	k_1 = 0.089, k_2 = -4.98E-4, k_3 = 0.076	k_1 = 0.068, k_2 = -5.07E-4, k_3 = 0.070	0.99	0.99

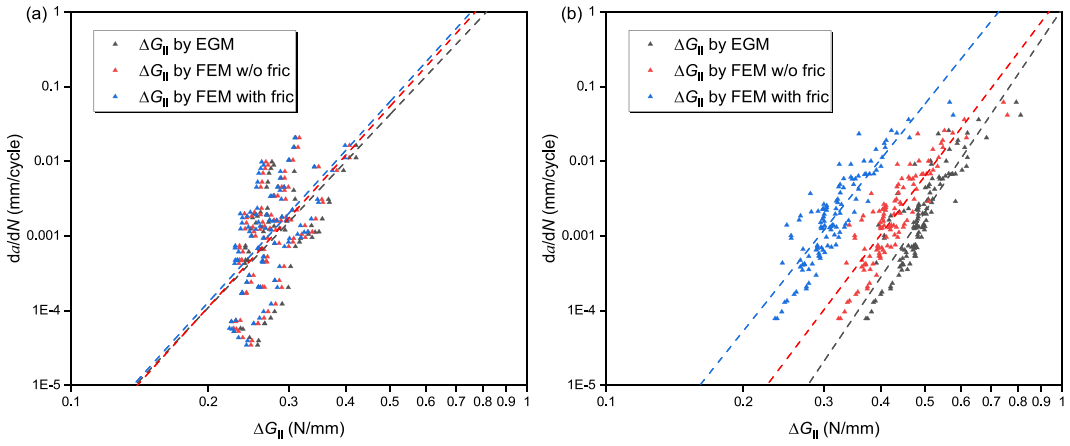

Fig. 15. Paris curves with SERR obtained by the EGM, FE model without friction and FE model with friction in (a) ENF and (b) 4ENF specimens.

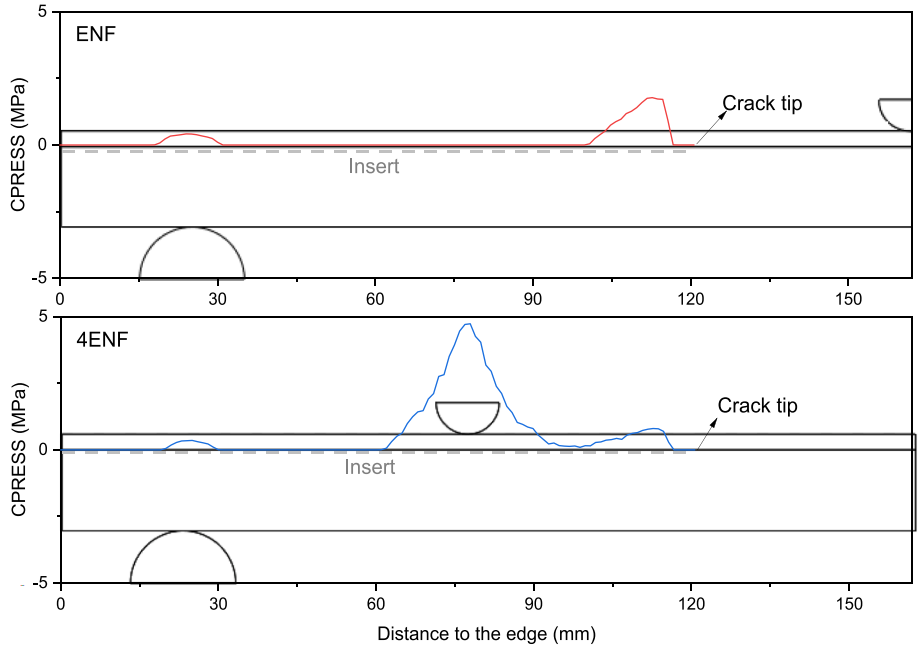

Fig. 16. Contact pressure at the cracked interface (P = 2kN).

scattering range. The higher *C* value of 4ENF specimens primarily stems from its slightly higher slope, i.e. *m* value.

5.2. Effect of steel yielding

In order to investigate the possible effect of steel yielding on the SERR values at the crack tip, the FE model described above is run with and without plasticity defined in the steel part, respectively. The friction coefficients and other parameters are kept the same. Comparison between FE models with and without plasticity defined in the steel part is shown in Fig. 18. Mode II SERR values are extracted at the crack tip of the initial crack and one longer crack for ENF and 4ENF, respectively. It can be seen that when plasticity exists at relatively high load level, the SERR values can be higher than those from FE model without plasticity defined. However, within the maximum load level appearing in the current study, namely below 1.2 kN for ENF tests and below 2.9 kN for 4ENF tests shown in Table 3, no difference can be found between FE models with and without plasticity, indicating that the influence of steel yielding is insignificant. It should be noted that the specimens were loaded cyclically during the tests, where cyclic plasticity may exists and cannot be considered in the current monotonically loaded FE model. That can be investigated in the future.

5.3. Fracture mode

This section checks and compares the mode mixity of ENF and 4ENF specimens. As the crack propagates during the tests, the steel and composite adherends exhibit different curvatures. This means that a small gap can be found between the arms at the cracked region. This may result from (1) plastic deformation of the steel during the test, as shown in Fig. 9; and/or (2) different flexural stiffness between steel and composites due to the asymmetry of the arms. To check its possible influence on the mode mixity, displacements of the specimens ENF-F-2 and 4ENF-D-1 are obtained from DIC and employed as boundary conditions of the FE models. As shown in Fig. 19, vertical displacements are extracted from two surface curves that are defined along the half-thickness of steel and composite adherends. The last DIC photo taken during the tests is chosen to extract the displacements for both ENF and 4ENF specimens, since the gap between steel and composite arms is found to be larger at later stages and have the most significant effect on

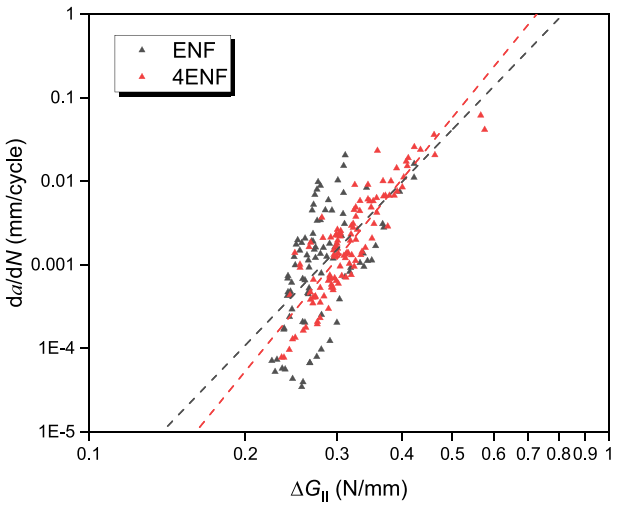

Fig. 17. Paris curves of ENF and 4ENF specimens obtained by FE model with friction.

inducing mode I component. Critical points of the steel and composite parts are selected from the experimental curves as boundary conditions: at the loading sections (BC-1 for ENF test, BC-1 and BC-4 for 4ENF test) and at the locations with largest relative displacement between steel and composite arms (BC-2 for the steel arm of ENF and 4ENF tests, and BC-3 for the composite arm of ENF and 4ENF tests).

The fracture modes are calculated by the VCCT and compared with those obtained from the model described in section 3.2. Fig. 20 shows the components of the fracture energy extracted from the same crack length and load level of these two types of models, one with boundary conditions defined according to the tests as in section 3.2 (BC-test) and one according to DIC (BC-DIC): a = 100 mm and P = 1.15 kN in ENF models; a = 188.5 mm and P = 2.30 kN in 4ENF models. As shown in Fig. 20 (a) and (c), mode II fracture dominates the crack growth in both ENF and 4ENF models. The mode III fracture component arises near the edges of the crack due to transverse shear deformation of the composites resulting from compressive stresses around the crack tip as shown in Fig. 21. The same phenomenon was also reported in Ref. [55]. But the mode III component generally remains below 20 % of the mode II components. The mode I fracture component is negligible for all the models except for ENF model with boundary conditions from DIC, where the mode I components result from the gap opening but is only 5 % of the mode II components. Overall, the fracture mode components from models with boundary conditions from the test and DIC overlap each

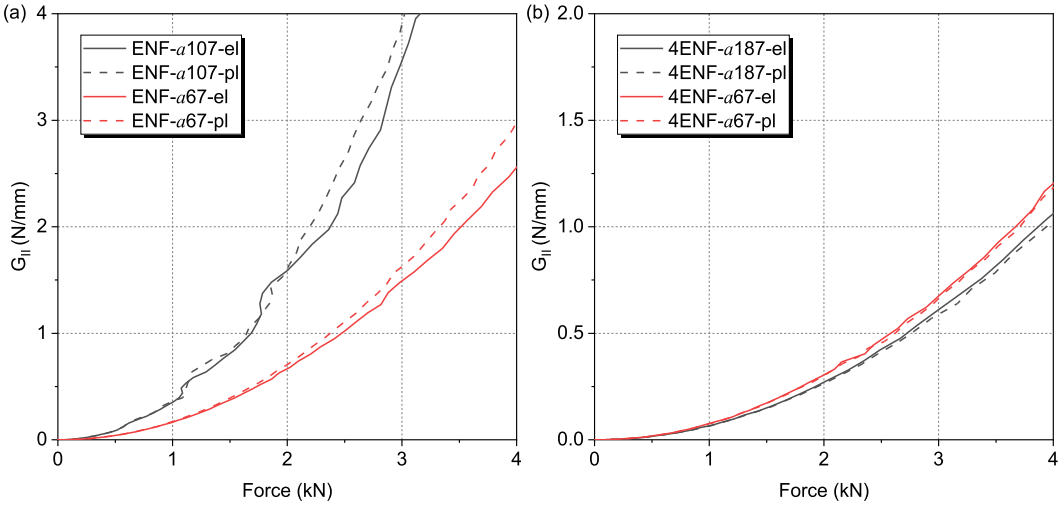

Fig. 18. Effect of steel yielding on the mode II SERR at the crack tip (a) ENF specimens with different crack lengths; (b) 4ENF specimens with different crack lengths.

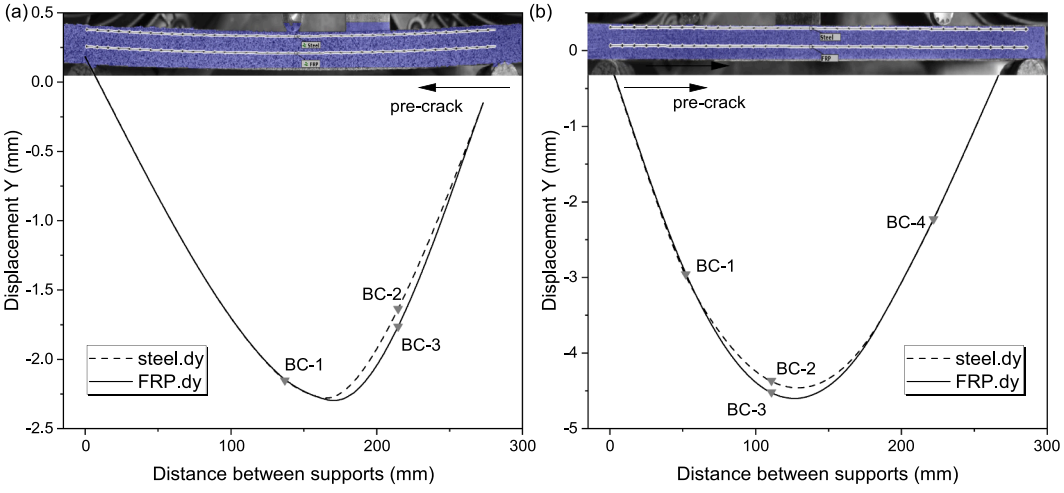

Fig. 19. Vertical displacement of steel and composite from DIC (a) ENF specimen; (b) 4ENF specimen.

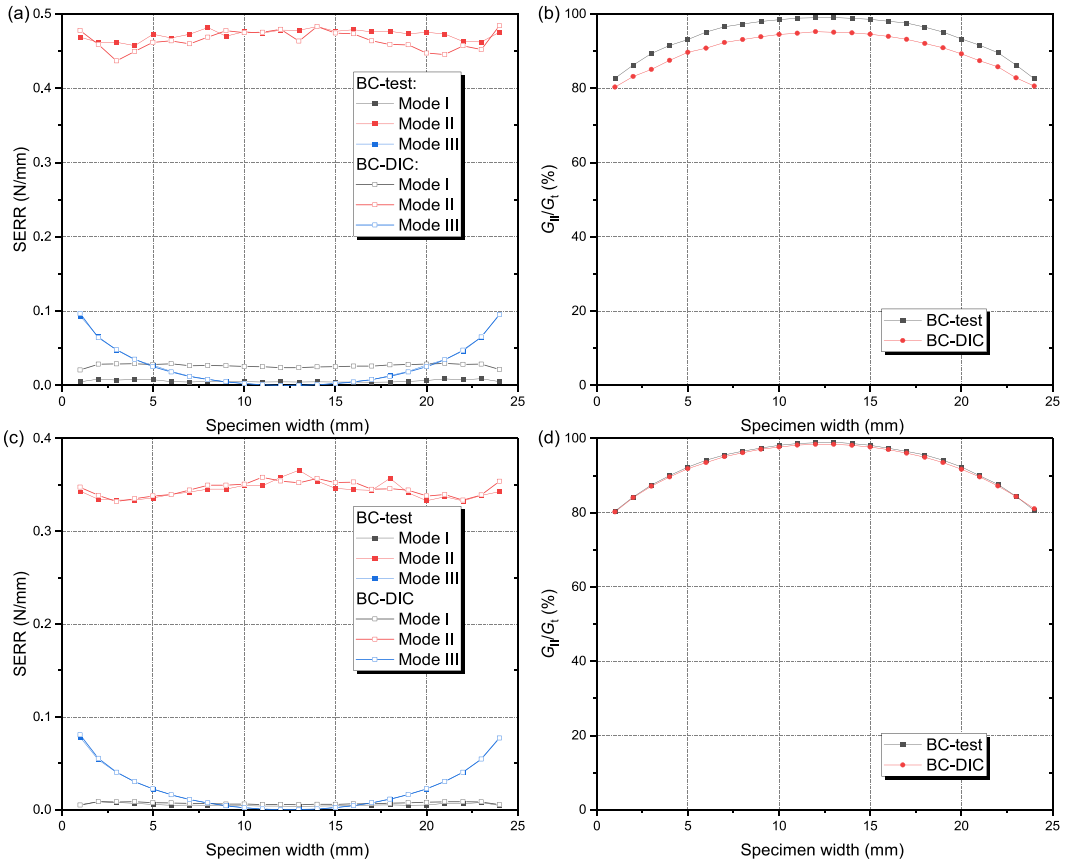

Fig. 20. Comparison between models with and without gap (a) Mode components of ENF specimen; (b) Mode II contributions of ENF specimen; (c) Mode components of 4ENF specimen; (d) Mode II contributions of 4ENF specimen.

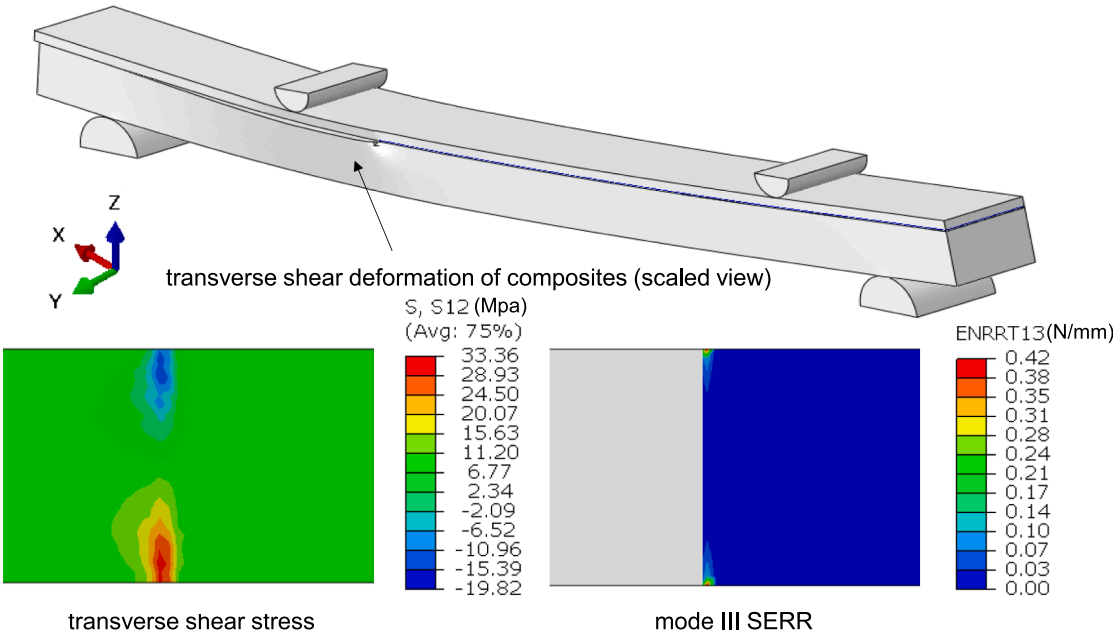

Fig. 21. Transverse shear deformation of composites and resulted shear stress, mode III SERR at the crack tip.

other.

The fracture mode ratio, namely the contribution of mode II component to the total SERR, or G_{II}/G_t, is compared in Fig. 20 (b) and (d). It is shown that the mode II fracture component contribute to almost 100 % of the SERR in the center of the specimen, but reduces near the edge due to presence of mode III component. The mode II fracture component contributes less in the ENF model with boundary conditions from DIC, but still remains above 90 % in the center and above 80 % near the edge of the crack. It can be concluded that the gap opening between steel and composite arms during the tests does not introduce in

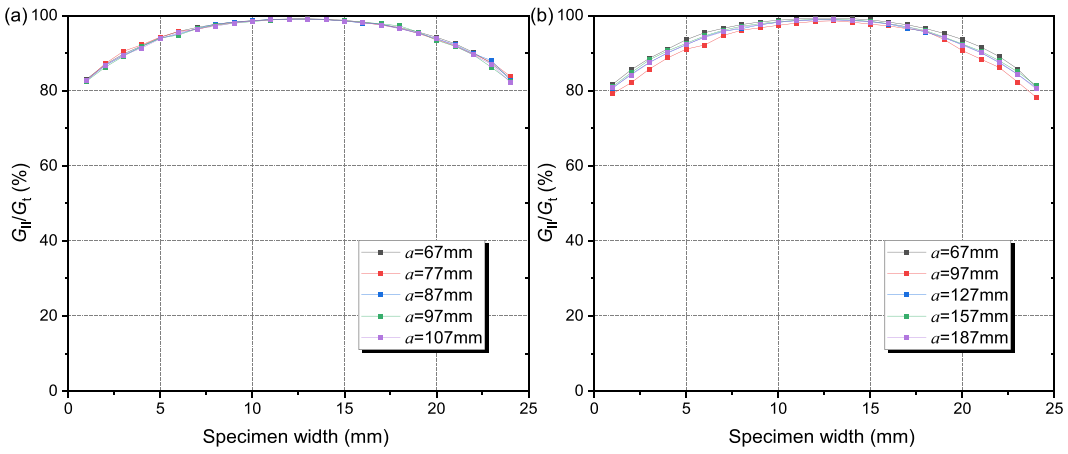

Fig. 22. Fracture mode ratio of a (a) ENF and (b) 4ENF specimen at different crack lengths.

significant mode I component to either ENF or 4ENF specimens. Therefore, it is reasonable to use the model with boundary conditions from the tests to calculate the SERR and the fracture mode ratios.

The fracture mode ratio is obtained at different crack lengths for ENF and 4ENF specimens respectively and are shown in Fig. 22. Results show that the fracture mode remains nearly constant in both ENF and 4ENF specimens as crack propagates.

5.4. Summative comparison between ENF and 4ENF test configurations

Based on the analysis from the previous sections, a summative comparison among different test configurations is presented in this section.

The first comparison is conducted between ENF and 4ENF specimens in terms of the maximum valid crack length. Using the same specimen geometry (320 mm length with a 67 mm pre-crack) and support device for the ENF and 4ENF tests, a crack in the ENF specimen can grow from 67 mm up to 122 mm, having the range of 55 mm, while in the 4ENF specimen the crack is allowed to grow up to 207 mm, resulting in a range of 150 mm. The larger space for crack growth in 4ENF tests gives the opportunity to measure a wider range of SERRs and ensure the full development of possible fracture process zone.

Another difference between ENF and 4ENF tests is the more pronounced geometrical nonlinearity and friction effects observed in 4ENF specimens, as discussed in section 5.1. A significant overestimation of the fatigue crack growth resistance may be obtained from 4ENF specimens when a linear elastic analysis, such as the EGM, is employed to calculate the SERR. A nonlinear FE analysis have the advantage of taking into account the relevant effects of geometrical nonlinearities and friction in the 4ENF test, but requires extensive work.

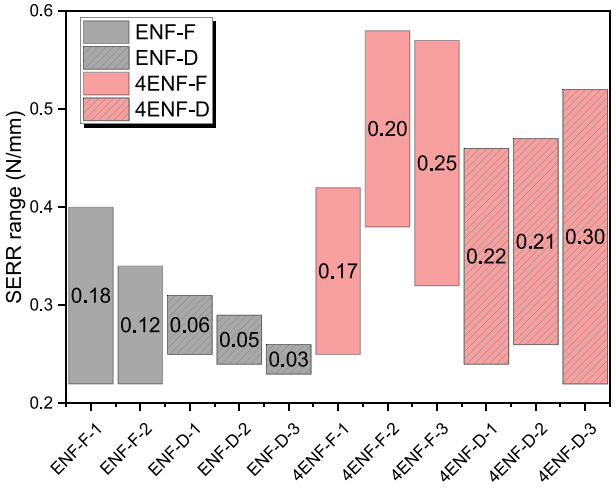

Fig. 23. SERR ranges covered by a single test (the absolute SERR range indicated in each column).

An efficient fatigue test method should cover as a large range of SERR as possible by a single test. Otherwise, more tests will be required with multiple force/displacement ranges to construct an accurate Paris curve. With the effects of nonlinearity and friction considered by the FE analysis, the SERR range covered by each test is summarised in Fig. 23. It can be seen in the current study that the displacement controlled ENF tests covered a smallest range of SERR, from around 0.2 to 0.3 N/mm. This occurs due to the decreasing force during the crack development, as discussed in section 4.2. On the other hand, the SERR of force controlled ENF tests shows an increasing trend as the crack grows. This gives the possibility to start with a low SERR and cover an wider range of SERR during the test. However, the force controlled ENF tests are found to be unstable. The highest SERR value depends on the largest crack length monitored before rapid failure. The maximum range of SERRs covered by the force control ENF tests is from 0.22 to 0.40 N/mm.

In the case of 4ENF tests, only the force level is required to determine the SERR by the EGM method. It is simpler to set a constant force level based on the target SERR range. Under the displacement controlled cyclic loading, the SERR decreases as the crack grows in 4ENF, due to gradual decrease of the specimen stiffness and therefore the applied force. The initial force level can be high enough to cover a wide range of SERRs, but it also needs to avoid rapid crack propagation in the beginning of the test. At the same time, if the initial displacement (load) is not high enough, the crack propagation can significantly reduce after initial period and stop before reaching the opposite loading point. The largest SERR range covered in this work is achieved by a single displacement controlled 4ENF test, from 0.22 to 0.52 N/mm by 4ENF-D-3. Under force control, the SERR development of 4ENF specimens can be manipulated, but the test procedure can be laborious. The range of SERRs covered by a force control 4ENF test remained between 0.25 and 0.60 N/mm.

6. Conclusions

In this paper, the mode II fatigue crack growth properties of a composite-to-steel bonded interface is characterised. Different test configurations, namely force and displacement controlled ENF tests, force and displacement controlled 4ENF tests, are carried out. The EGM and the VCCT are employed to obtain the SERR at the crack tip. The effects of geometrical nonlinearity, friction between fractured surfaces, steel yielding as well as the fracture mode ratio are investigated. Based on the experimental and FE analysis performed in this study, the following conclusions can be drawn:

- The displacement controlled ENF tests cover the narrowest SERR range by a single test (e.g. only 0.2 to 0.3 N/mm) due to the non-monotonic evolution of SERR. The force controlled ENF test method covers decent range of SERR (0.22 to 0.40 N/mm), has limited scattering but is prone to instable crack propagation;
- The displacement controlled 4ENF tests provide lower scattering of the results than the ENF tests, covers relatively wide range of SERRs in a single test (e.g. approx. 0.22 to 0.52 N/mm), and it requires less labour in testing;
- The force controlled 4ENF test method provides opportunity to manipulate the range of SERR and can avoid the scattering of the test results by containing the averaging information for each force level, but requires intensive labour work. It shows potential if real-time load evaluation and calibration can be automated;
- The geometrical nonlinearity and friction effects are more pronounced in 4ENF tests, leading to a higher fatigue crack propagation resistance when calculating SERRs by the EGM. The nonlinear effects can be taken into account by a nonlinear FE model based on VCCT where friction at the interface is explicitly considered. The results from 4ENF tests adjusted on the basis of FE model overlap well with ENF tests;
- A non-equivalent deflection between steel and composite arms leads to an opening gap between the cracked surfaces during the test. However, this behaviour has no significant influence on the fracture mode for either ENF or 4ENF test. The mode II fracture component dominates the crack growth in both test methods, namely contributes more than 80 %-90 % of the total SERR.

Current study focuses on the fatigue crack propagation stage. The threshold SERR values are not covered by this study but needs to be determined in the future. Monotonic load is applied in the FE model to calculate the SERR values but further study is required to investigate the influence of cyclic plastic in the steel adherend on the SERR values. Additionally, the present study compared different test configurations by fixing the testing parameters, e.g. specimen geometry and test set-up. Some drawbacks of a certain test configuration can be mitigated by changing these testing parameters. For instance, the friction effect of 4ENF specimens can be reduced by shortening the distance between two loading points. The influence of testing parameters is out of scope of the present study and will be further investigated.

CRediT authorship contribution statement

Weikang Feng: Data curation, Formal analysis, Investigation, Visualization, Writing – original draft. **Marcio Moreira Arouche:** Data curation, Investigation, Validation, Writing – review & editing. **Marko Pavlovic:** Conceptualization, Funding acquisition, Methodology, Project administration, Supervision.

Declaration of competing interest

The authors declare that they have no known competing financial interests or personal relationships that could have appeared to influence the work reported in this paper.

Data availability

The authors are unable or have chosen not to specify which data has been used.

Acknowledgments

The authors would like to express their gratitude to RVO for the financial support with Topsector Energiesubsidie van het Ministerie van Economische Zaken through WrapNode-I project, and Tree Composites B.V. for the production of specimens. Acknowledgements are also made towards Siyuan Hou for the assistance of conducting experiments and Tim In het Panhuis for production of the specimens. The first author also would like to express his gratitude for the financial support from China Scholarship Council (CSC) under grant number of 201906260300.

References

[1] Vlot A, Gunnink JW. Fibre Metal Laminates - An Introduction. Springer Netherlands; 2001. https://doi.org/10.1007/978-94-010-0995-9.
[2] Dlugosch M, Fritsch J, Lukaszewicz D, Hiermaier S. Experimental investigation and evaluation of numerical modeling approaches for hybrid-FRP-steel sections under impact loading for the application in automotive crash-structures. Compos Struct 2017;174:338–47. https://doi.org/10.1016/J.COMPSTRUCT.2017.04.077.
[3] Zhao XL, Zhang L. State-of-the-art review on FRP strengthened steel structures. Eng Struct 2007;29:1808–23. https://doi.org/10.1016/j.engstruct.2006.10.006.
[4] Colombi P. Reinforcement delamination of metallic beams strengthened by FRP strips: Fracture mechanics based approach. Eng Fract Mech 2006;73:1980–95. https://doi.org/10.1016/j.engfracmech.2006.03.011.
[5] Bocciarelli M, Colombi P, Fava G, Poggi C. Prediction of debonding strength of tensile steel/CFRP joints using fracture mechanics and stress based criteria. Eng Fract Mech 2009;76:299–313. https://doi.org/10.1016/j.engfracmech.2008.10.005.
[6] Wang W, De Freitas ST, Poulis JA, Zarouchas D. A review of experimental and theoretical fracture characterization of bi-material bonded joints. Compos Part B Eng 2021;206:108537. https://doi.org/10.1016/j.compositesb.2020.108537.
[7] Feng W, Pavlovic M. Fatigue behaviour of non-welded wrapped composite joints for steel hollow sections in axial load experiments. Eng Struct 2021;249:113369. https://doi.org/10.1016/J.ENGSTRUCT.2021.113369.
[8] Feng W, He P, Pavlovic M. Combined DIC and FEA method for analysing debonding crack propagation in fatigue experiments on wrapped composite joints. Compos Struct 2022;297:115977. https://doi.org/10.1016/J.COMPSTRUCT.2022.115977.
[9] He P, Pavlovic M. Failure modes of bonded wrapped composite joints for steel circular hollow sections in ultimate load experiments. Eng Struct 2022;254:113799. https://doi.org/10.1016/j.engstruct.2021.113799.
[10] Sourisseau, Quentin; Lepretre E, Chataigner S, Chapeleau X, Deydier M, Paboeuf S. A new adhesively bonded composite repair for offshore steel structures: strength assessment and fatigue. 11th Int. Conf. FRP Compos. Civ. Eng., Rio de Janeiro: 2023.
[11] Delbariani-Nejad A, Malakouti M, Farrokhabadi A. Reliability analysis of metal-composite adhesive joints under debonding modes I, II, and I/II using the results of experimental and FEM analyses. Fatigue Fract Eng Mater Struct 2019;42:2644–62. https://doi.org/10.1111/FFE.13078.
[12] ASTM D5528–01. Standard test method for mode I interlaminar fracture toughness of unidirectional fiber-reinforced polymer matrix composites. Am Stand Test Methods 2014;03:1–12.
[13] Zambelis G, Da Silva BT, Klinkova O, Tawfiq I, Lanouette C. Evaluation of the energy release rate in mode I of asymmetrical bonded composite/metal assembly. Eng Fract Mech 2018;190:175–85. https://doi.org/10.1016/j.engfracmech.2017.12.007.
[14] Wang W, Lopes Fernandes R, Teixeira De Freitas S, Zarouchas D, Benedictus R. How pure mode I can be obtained in bi-material bonded DCB joints: A longitudinal strain-based criterion. Compos Part B Eng 2018;153:137–48. https://doi.org/10.1016/j.compositesb.2018.07.033.
[15] Qiao Y, Merkel DR, Nickerson EK, Shin Y, Seffens RJ, Ortiz A, et al. Mode I tensile fracture behavior of adhesively-bonded metal–metal, metal–CFRP, and CFRP–CFRP bi-material combinations analyzed by size effect method. Compos Part A Appl Sci Manuf 2022;160:107025. https://doi.org/10.1016/J.COMPOSITESA.2022.107025.
[16] Dantas R, Mohabeddine A, de Moura M, Moreira R, Lesiuk G, Correia J, et al. Fracture Characterization of Hybrid Bonded Joints (CFRP/Steel) for Pure Mode I. Struct. Integr., vol. 25, Springer, Cham; 2022, p. 215–33. https://doi.org/10.1007/978-3-030-91847-7_21.
[17] Wang WX, Nakata M, Takao Y, Matsubara T. Experimental investigation on test methods for mode II interlaminar fracture testing of carbon fiber reinforced composites. Compos Part A Appl Sci Manuf 2009;40:1447–55. https://doi.org/10.1016/J.COMPOSITESA.2009.04.029.
[18] Carlsson LA, Gillespie JW, Pipes RB. On the Analysis and Design of the End Notched Flexure (ENF) Specimen for Mode II Testing. J Compos Mater 1986;20:594–604. https://doi.org/10.1177/002199838602000606.
[19] ASTM D7905. Standard test method for determination of the mode II interlaminar fracture toughness of unidirectional fiber-reinforced polymer matrix composites. ASTM 2014:1–18. https://doi.org/10.1520/D7905_D7905M-19E01.
[20] Wang J, Qiao P. Novel beam analysis of end notched flexure specimen for mode-II fracture. Eng Fract Mech 2004;71:219–31. https://doi.org/10.1016/S0013-7944(03)00096-1.
[21] Shindo Y, Sato T, Narita F, Sanada K. Mode II interlaminar fracture and damage evaluation of GFRP woven laminates at cryogenic temperatures using the 4ENF specimen. J Compos Mater 2008;42:1089–101. https://doi.org/10.1177/0021998308090451.
[22] Sun X, Davidson BD. Numerical evaluation of the effects of friction and geometric nonlinearities on the energy release rate in three- and four-point bend end-notched flexure tests. Eng Fract Mech 2006;73:1343–61. https://doi.org/10.1016/J.ENGFRACMECH.2005.11.007.

[23] Schuecker C, Davidson BD. Effect of friction on the perceived mode II delamination toughness from three- and four-point bend end-notched flexure tests. ASTM Spec Tech Publ 2000:334–44. https://doi.org/10.1520/stp14518s.
[24] Schuecker C, Davidson BD. Evaluation of the accuracy of the four-point bend end-notched flexure test for mode II delamination toughness determination. Compos Sci Technol 2000;60:2137–46. https://doi.org/10.1016/S0266-3538(00)00113-5.
[25] Davidson BD, Sun X, Vinciquerra AJ. Influences of friction, geometric nonlinearities, and fixture compliance on experimentally observed toughnesses from three and four-point bend end-notched flexure tests. J Compos Mater 2007; 41:1177–96. https://doi.org/10.1177/0021998306067304.
[26] Davidson BD, Sun X. Effects of Friction, Geometry, and Fixture Compliance on the Perceived Toughness from Three-and Four-Point Bend End-Notched Flexure Tests. J Reinf Plast Compos 2005;24:1611–28. https://doi.org/10.1177/0731684405050402.
[27] Dadej K, Bieniaś J, Valvo PS. Experimental testing and analytical modeling of asymmetric end-notched flexure tests on glass-fiber metal laminates. Metals (Basel) 2020;10. https://doi.org/10.3390/MET10010056.
[28] Valvo PS. On the calculation of energy release rate and mode mixity in delaminated laminated beams. Eng Fract Mech 2016;165:114–39. https://doi.org/10.1016/j.engfracmech.2016.08.010.
[29] Sundararaman V, Davidson BD. An Unsymmetric End-Notched Flexure Test for Interfacial Fracture Toughness Determination. Eng Fract Mech 1998;60:361–77. https://doi.org/10.1016/S0013-7944(98)00017-4.
[30] Jiang Z, Fang Z, Wan S, Xie K. Mode-II fracture behavior evaluation for adhesively bonded pultruded GFRP/steel joint using four-point bending test. Thin-Walled Struct 2021;167:108130. https://doi.org/10.1016/J.TWS.2021.108130.
[31] Shahverdi M, Vassilopoulos AP, Keller T. Mixed-Mode I/II fracture behavior of asymmetric adhesively-bonded pultruded composite joints. Eng Fract Mech 2014; 115:43–59. https://doi.org/10.1016/J.ENGFRACMECH.2013.11.014.
[32] Ouyang Z, Li G. Nonlinear interface shear fracture of end notched flexure specimens. Int J Solids Struct 2009;46:2659–68. https://doi.org/10.1016/J.IJSOLSTR.2009.02.011.
[33] Matsubara G, Ono H, Tanaka K. Mode II fatigue crack growth from delamination in unidirectional tape and satin-woven fabric laminates of high strength GFRP. Int J Fatigue 2006;28:1177–86. https://doi.org/10.1016/J.IJFATIGUE.2006.02.006.
[34] Brunner AJ, Stelzer S, Pinter G, Terrasi GP. Mode II fatigue delamination resistance of advanced fiber-reinforced polymer-matrix laminates: Towards the development of a standardized test procedure. Int J Fatigue 2013;50:57–62. https://doi.org/10.1016/j.ijfatigue.2012.02.021.
[35] Carreras L, Renart J, Turon A, Costa J, Essa Y, Martin de la Escalera F. An efficient methodology for the experimental characterization of mode II delamination growth under fatigue loading. Int J Fatigue 2017;95:185–93. https://doi.org/10.1016/J.IJFATIGUE.2016.10.017.
[36] Shindo Y, Takeda T, Narita F, Saito N, Watanabe S, Sanada K. Delamination growth mechanisms in woven glass fiber reinforced polymer composites under Mode II fatigue loading at cryogenic temperatures. Compos Sci Technol 2009;69:1904–11. https://doi.org/10.1016/J.COMPSCITECH.2009.04.010.
[37] Bieniaś J, Dadej K. Fatigue delamination growth of carbon and glass reinforced fiber metal laminates in fracture mode II. Int J Fatigue 2020;130:105267. https://doi.org/10.1016/J.IJFATIGUE.2019.105267.
[38] Adamos L, Tsokanas P, Loutas T. An experimental study of the interfacial fracture behavior of Titanium/CFRP adhesive joints under mode I and mode II fatigue. Int J Fatigue 2020;136:105586. https://doi.org/10.1016/j.ijfatigue.2020.105586.
[39] Arouche MM, Teixeira de Freitas S, de Barros S. Evaluation of the strain-based partitioning method for mixed-mode I+II fracture of bi-material cracks. J Adhes 2022;98:577–605. https://doi.org/10.1080/00218464.2021.1981297.
[40] Arouche MM, Wang W, Teixeira de Freitas S, de Barros S. Strain-based methodology for mixed-mode I+II fracture: A new partitioning method for bi-material adhesively bonded joints. J Adhes 2019;95:385–404. https://doi.org/10.1080/00218464.2019.1565756.
[41] Yan R, El Bamby H, Veljkovic M, Xin H, Yang F. A method for identifying the boundary of regions in welded coupon specimens using digital image correlation. Mater Des 2021;210:110073. https://doi.org/10.1016/J.MATDES.2021.110073.
[42] BS EN ISO. 527-1:2019 Plastics. Determination of tensile properties. General principles 2019.
[43] British Standards Institution. Fibre-rinforced plastic composites - Determination of compressive properties in the in-plane direction (ISO 14126:1999). Iso 2001;2001: 1–25.
[44] International Organization for Standardization. ISO 14129:1997, Fibre-reinforced plastic composites - Determination of the in-plane shear stress/shear strain response, including the in-plane shear modulus and strength, by the plus or minus 45 degree tension test method 2007.
[45] He P. Debonding Resistance of CHS Wrapped Composite X-Joints. Delft University of Technology; 2023.
[46] Hou S. Experimental study of Mode II fatigue test methodology for composite-to-steel interface. Delft University of Technology; 2023.
[47] Zhu M, Gorbatikh L, Fonteyn S, Van Hemelrijck D, Pyl L, Carrella-Payan D, et al. Digital image correlation assisted characterization of Mode I fatigue delamination in composites. Compos Struct 2020;253:112746. https://doi.org/10.1016/j.compstruct.2020.112746.
[48] Huo X, Luo Q, Li Q, Sun G. Measurement of fracture parameters based upon digital image correlation and virtual crack closure techniques. Compos Part B Eng 2021; 224:109157. https://doi.org/10.1016/J.COMPOSITESB.2021.109157.
[49] Williams JG. On the calculation of energy release rates for cracked laminates. Int J Fract 1988.101–19.;1988(362):36. https://doi.org/10.1007/BF00017790.
[50] Rybicki EF, Kanninen MF. A finite element calculation of stress intensity factors by a modified crack closure integral. Eng Fract Mech 1977;9:931–8. https://doi.org/10.1016/0013-7944(77)90013-3.
[51] Abaqus Unified FEA - SIMULIA™ by Dassault Systèmes® n.d. https://www.3ds.com/products-services/simulia/products/abaqus/ (accessed May 12, 2022).
[52] Gillespie JW, Carlsson LA, Pipes RB. Finite element analysis of the end notched flexure specimen for measuring mode II fracture toughness. Compos Sci Technol 1986;27:177–97. https://doi.org/10.1016/0266-3538(86)90031-X.
[53] ASTM E647−13. Standard Test Method for Measurement of Fatigue Crack Growth Rates. Am Soc Test Mater 2014:1–50. https://doi.org/10.1520/E0647-15E01.2.
[54] Martin RH, Davidson BD. Mode II fracture toughness evaluation using four point bend, end notched flexure test. Plast Rubber Compos Process Appl 1999;28:401–6. https://doi.org/10.1179/146580199101540565.
[55] Gliszczynski A, Wiącek N. Experimental and numerical benchmark study of mode II interlaminar fracture toughness of unidirectional GFRP laminates under shear loading using the end-notched flexure (ENF) test. Compos Struct 2021;258: 113190. https://doi.org/10.1016/j.compstruct.2020.113190.